Geomechanics and Engineering, *Vol. 28, No. 6 (2022) 599-611*
https://doi.org/10.12989/gae.2022.28.6.599

Optimised neural network prediction of interface bond strength for GFRP tendon reinforced cemented soil

Genbao Zhang[1,3], Changfu Chen[4,5], Yuhao Zhang[6], Hongchao Zhao[7], Yufei Wang[*2] and Xiangyu Wang[8]

[1]*College of Civil Engineering, Hunan City University, Yiyang, Hunan 413000, PRC*
[2]*Institute for Smart City of Chongqing University in Liyang, Chongqing University, Jiangsu, 213300, China*
[3]*Hunan Engineering Research Center of Structural Safety and Disaster Prevention for Urban Underground Infrastructure, Yiyang, Hunan 413000, PRC*
[4]*Key Laboratory of Building Safety and Energy Efficiency of the Ministry of Education, Hunan University, Changsha, Hunan 410082, PRC*
[5]*College of Civil Engineering, Hunan University, Changsha, Hunan 410082, PRC*
[6]*School of Civil and Environmental Engineering, University of New South Wales, Sydney, NSW 2052, Australia*
[7]*School of Geology and Mining Engineering, Xinjiang University, Urumchi 830000, China*
[8]*School of Design and Built Environment, Curtin University, Perth, WA 6102, Australia*

(Received May 30, 2021, Revised January 31, 2022, Accepted February 4, 2022)

Abstract. Tendon reinforced cemented soil is applied extensively in foundation stabilisation and improvement, especially in areas with soft clay. To solve the deterioration problem led by steel corrosion, the glass fiber-reinforced polymer (GFRP) tendon is introduced to substitute the traditional steel tendon. The interface bond strength between the cemented soil matrix and GFRP tendon demonstrates the outstanding mechanical property of this composite. However, the lack of research between the influence factors and bond strength hinders the application. To evaluate these factors, back propagation neural network (BPNN) is applied to predict the relationship between them and bond strength. Since adjusting BPNN parameters is time-consuming and laborious, the particle swarm optimisation (PSO) algorithm is proposed. This study evaluated the influence of water content, cement content, curing time, and slip distance on the bond performance of GFRP tendon-reinforced cemented soils (GTRCS). The results showed that the ultimate and residual bond strengths were both in positive proportion to cement content and negative to water content. The sample cured for 28 days with 30% water content and 50% cement content had the largest ultimate strength (3879.40 kPa). The PSO-BPNN model was tuned with 3 neurons in the input layer, 10 in the hidden layer, and 1 in the output layer. It showed outstanding performance on a large database comprising 405 testing results. Its higher correlation coefficient (0.908) and lower root-mean-square error (239.11 kPa) were obtained compared to multiple linear regression (MLR) and logistic regression (LR). In addition, a sensitivity analysis was applied to acquire the ranking of the input variables. The results illustrated that the cement content performed the strongest influence on bond strength, followed by the water content and slip displacement.

Keywords: back propagation neural network; cemented soil; element pullout test; glass fibre reinforced polymer reinforcement; interface bond strength; machine learning; particle swarm optimisation

1. Introduction

As an imperative binding agent, cement is widely used in geotechnical engineering to improve and stabilise the ground with soft clay or polluted silt particularly (Kitazume 2013, Qin *et al.* 2020, Alam *et al.* 2021). Cement filling the pores in soft soils employing soil mixing and jet grouting yields pozzolanic activities to produce cement-soil composite. The properties of this composite are much improved than its ingredients alone (Han 2014, Li *et al.* 2020).

The combination of reinforcements into cement-soil composites is proposed in excavation support and cutting off surface water to sustain the inevitable lateral earth pressure (Shen *et al.* 2013, Luo *et al.* 2020, Xu *et al.* 2021).

One traditional method is to utilize rebar reinforcement as part of the structure combined with the cement-soil matrix to withstand the exterior load. However, the rebar is bound to corrode during its service period which will lead to the deteriorated performance of the composite, particularly in permanent structures (Chen *et al.* 2018, Wang *et al.* 2019, Wang *et al.* 2022). To address this problem, GFRP tendons are employed to substitute the steel rebars due to their high affordability and outstanding engineering property (Yan and Lin 2016, Wang *et al.* 2018, Fan *et al.* 2021).

The interface bond property of GTRCS is essential since it presents the pullout ability, in agreement with reinforced concrete (Tepfers *et al.* 2000, Ju *et al.* 2020). In many cases, failures are caused by the bonding surface detachment before the tendon reaches its ultimate strength. However,

*Corresponding author, Professor, Ph.D.
E-mail: wangyf0113_suz@163.com

ISSN: 2005-307X (Print), 2092-6219 (Online)

the failure mode correlated to the interface bond strength is indistinct, leading to inadequate design guidelines of reinforced cement-soil structures (CECS147 2016, Xie *et al.* 2020). Moreover, previous research mainly focuses on cemented soil's hydraulic characteristics and mechanical properties (Horpibulsuk *et al.* 2003, Chew *et al.* 2004, Abedini and Zhang 2021). Few reports mention the bond performance between soil and GFRP reinforcements (Timoney and Mccabe 2017, Zhao *et al.* 2020). This hinders the utilization of GFRP tendons in cemented soils in practice.

Cementitious solid, soil solid, and water are the three main components of cement-soil composite, which largely influence its mechanical properties (Timoney *et al.* 2012, Kitazume 2013). Besides, the interface bond strength of GTRCS is correlated to the relative slip displacement (S_p) between cemented soil and tendons (Zhu *et al.* 2021). Consequently, water content (C_w), cement content (C_c), curing time (T_c), and S_p are four variables in this study. Due to complicated facilities and abundant samples prepared in an experimental environment, such a process was expensive and time-consuming. Moreover, the traditional data analysing methodologies have drawbacks in error control and obtaining the best mix proportion under multivariable conditions (Liu *et al.* 2015, Mou and Bai 2018, Hou *et al.* 2021). Although multiple linear regression (MLR) and logistic regression (LR) are extensively employed, the curse of dimensionality and co-linearity susceptibility resulting in an inaccurate simulation is still common (Fernández-Martínez *et al.* 2020, Medvedeva *et al.* 2020). Thereby, improved models are in great demand to help study interface bond strength.

Nowadays, artificial intelligence (AI) techniques are commonly applied in the field of building materials and construction to build the bridge between inputs and outputs (Abedini *et al.* 2020, Alam *et al.* 2020, Zhang *et al.* 2021, Zhang *et al.* 2021, Feng *et al.* 2022). For instance, the artificial neural network (ANN) shows excellence in the prediction of concrete strength (Sun *et al.* 2021). The random forest (RF) vote to forecast concrete conductivity as an Ensemble Learning Method (Sun *et al.* 2021). The support vector regression (SVR)'s terrific ability to generalize and calculate makes it popular in the information mining field (Sun *et al.* 2021). Using AI techniques to process data in complicated experimental tasks saves both time and money (Sun *et al.* 2019, Gholipour *et al.* 2020, Sun *et al.* 2021). Back propagation neural network is of the most versatility and prevalence among all these techniques. Because it is programmed easily and fast since programmers only need to adjust the neural network configuration (Chandwani *et al.* 2015, Zhao *et al.* 2021). Its large-scale parallel computation provides the platform to assess any objects constantly with high efficiency. Thereby, BPNN has been in common application to forecast and compare mechanical characteristics of various materials.

Although BPNN is in wide use, devising BPNN still consists of numerous arduous trial-and-error methodologies. The quantity of hidden layers and neurons in each of them are two major hyperparameters affecting BPNN characteristics directly (Sun *et al.* 2019). It costs plenty of effort and time to form the BPNN framework with optimal hyperparameters which hinders the subsequent process (Sun *et al.* 2020, Zhang *et al.* 2020, Zheng *et al.* 2020). Thereby, the particle swarm optimization (PSO) algorithm was used in this research to adjust the BPNN framework. In general, the PSO is a simple heuristic algorithm and stochastic technique (Abido *et al.* 2002). Its mechanism is well balanced and is flexible to suit and boost global and local search. In addition, compared to other optimization techniques, it has higher computational efficiency, demands less memory, and is performed easier (Medvedeva *et al.* 2020). With the combination of these two, the number of hidden layers, the number of neurons in them, and the connection weights were adjusted to further save time and labor. Owning to the outstanding robustness, fast convergence, and satisfying distributed ability of the PSO algorithm, the improved framework predicted bond strength better.

In summary, pullout tests were carried out in this study to explore the relationship between the interface bond strength (T_p) of GTRCS and four variables (C_w, C_c, T_c, and S_p), which are also the four features in machine learning. In total, 405 generated testing results served as the dataset to train the high accurate PSO-BPNN model. Testing and training datasets with the optimal BPNN were built to study the error conditions in both sets. Besides, computed correlation coefficients were also applied to evaluate the relationship between the forecasted and measured T_p outcome generated by such a model. Eventually, a sensitivity analysis was applied to acquire the ranking of the input variables.

2. Experimental programs

2.1 Materials

Soil equipping 40%-80% natural water content was gathered from the floodplain, adjacent to the junction of Xiangjiang and Jinjiang River in Changsha, China. Soil particles were air-dried and ground in a machine before being sifted out. To obtain uniform granularity, only particles less than 5 millimeters in diameter were retained and the particle-size distribution is shown in Fig. 1. The ordinary Portland cement was utilized as the main binder composition with a strength grade of 42.5. GFRP tendon was 230mm in height to form GTRCS as pullout specimens. The characteristics of the soil sample, cement, and GFRP tendon are presented in Table 1 (Chen *et al.* 2020).

2.2 Mixture design

As mentioned above, C_w, C_c, and T_c are three variables that significantly influence the properties of GTRCS. Water content defines the proportion of the water to dry soil mass. Areas where cemented stabilization are widely employed usually feature clay with C_w near the liquid limit (normally ranging from 50% to 90%). Cement content is presented as the mass ratio of cement to the total of water and dry soil. It was designed specifically to offer optimal stabilization

Table 1 Materials used in the experimental program (Chen *et al.* 2020)

Properties	Values
Soil sample	
Specific gravity	2.705
Natural water content (%)	30-90
Liquid limit (%)	58.1
Plasticity limit (%)	28.6
Cement	
Type	P.O 42.5
Specific gravity (t/m³)	3.0-3.2
Compressive strength (MPa)	≥42.5 (28-day)
Normal consistency (%)	27
GFRP reinforcement	
Type	GFRP tendon
Rib spacing (mm)	10.1
Tensile strength (MPa)	466
Outer diameter (mm)	16.8
Inner diameter (mm)	15
Young's modulus (GPa)	40

Table 2 Influence variables with all levels used in the experimental project

Influence factor	Number of levels	Magnitude	Minimum	Maximum	Mean
Water content C_w (%)	3	50, 70, 90	50	90	70
Cement content C_c (%)	3	6, 18, 30	6	30	18
Curing duration T_c (days)	3	7, 14, 28	7	28	16.3
Slip displacement S_p (mm)	15	0.5,1,1.5,2,2.5,3,3.5,5,7,9,11,13,15,17,20	0.5	20	7.4

efficiency and adequate workability, usually between 6% to 30% (R. Babasaki 1996, Å hnberg 2006, Wang *et al.* 2021). Besides, properties of composites cured for 15 to 30 days are widely used in case of practical problems such as tight schedules (Han 2014, Xu *et al.* 2020). Hence, three stepwise increasing levels were chosen for C_w, C_c, and T_c with specific details shown in Table 2. In total, 27 GTRCS specimens were prepared in this study (3 levels for C_c × 3 levels for C_w × 3 levels for T_c).

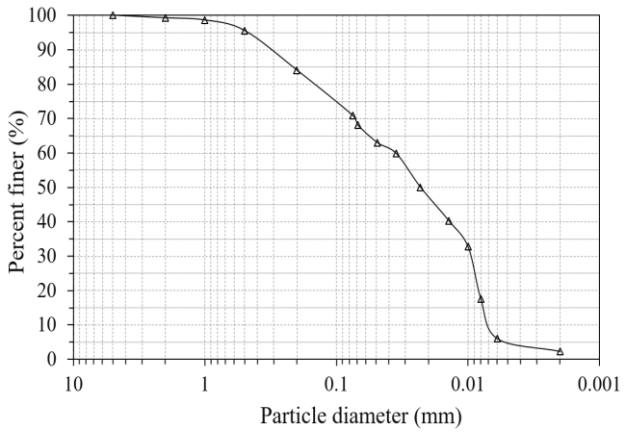

Fig. 1 Particle size distribution of soil sample (Chen *et al.* 2020)

2.3 Sample preparation

Cement-soil composites were prepared by mixing soil and cement samples for 60 seconds. Later, water was added and composites were mixed for another 480 seconds. GFRP bar was installed in the middle of the pullout cell, as presented in Fig. 2. The cells' bottoms were sealed with paper plates in case of leaking and their internal surfaces were lubricated to effectively limit the boundary friction. Then, cemented soils were placed into the pullout cell and vibrated to compact the microstructure with an even density. Subsequently, each cell was stored in sealed plastic bags for a preset curing time. After 7-day curing, paper plates were detached to avoid extra adhesion.

2.4 Pullout test

The pullout load was conducted to the GTRCS specimen tendon employing a pile interface friction testing system (PIFTS) and its conformation is presented in Fig. 3. The GTRCS specimen was installed on the traveling platform and the tendon's top was fixed to the load cell. The traveling platform supplied the pullout force on the tendon. It was fixed tightly with a constraining plate using screws to guarantee proper interface shear displacement while the platform was descending 1.0 mm/min. The load and corresponding displacement were recorded by a load cell and a linear variable differential transformer (LVDT),

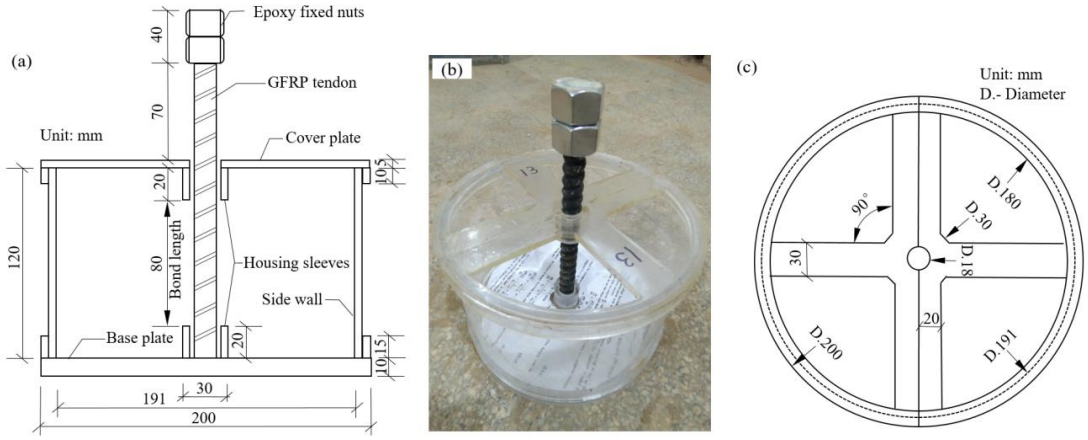

Fig. 2 Setup of pullout cell: (a) diagram of cross-sectional elevation, (b) 3D view of cell; and (c) diagram of cross-sectional plan (Chen *et al.* 2020)

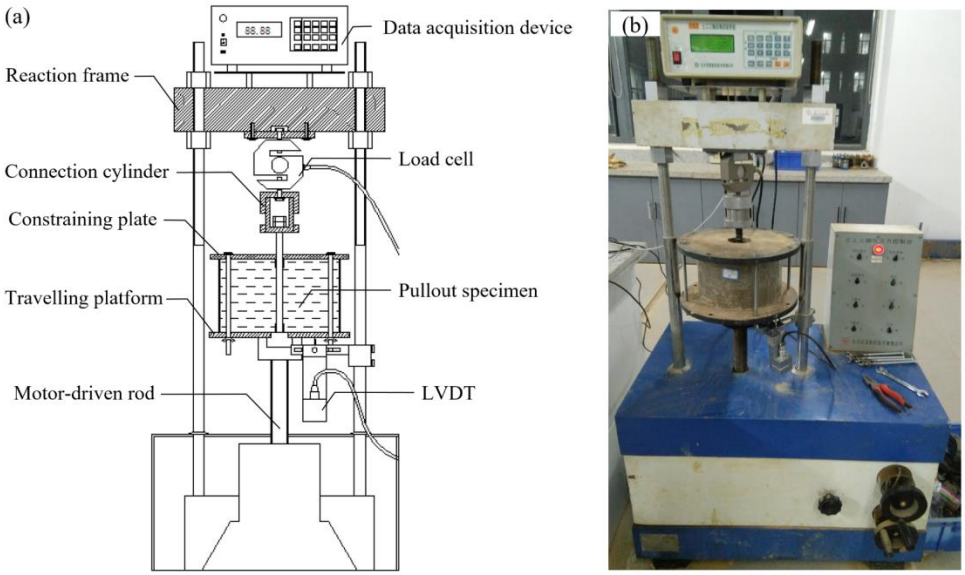

Fig. 3 Pullout loading equipment: (a) diagram of setup; and (b) view in the lab (Chen *et al.* 2020)

respectively. The loading process was ended as soon as the platform got a 20-mm displacement which sufficiently led to a complete detachment between the cemented soils and tendon (Chen *et al.* 2018). Eventually, the pullout strength can be calculated at 15 interface slip distances, shown in Appendix.

3. Machine learning methods

3.1 Back propagation neural network

The relationships between inputs (affecting variables) and outputs (interface bond strength) in this case were modeled using an artificial neural network. Generally, multiple inputs are corresponding to one single output in a neuron and neurons are divided into groups in each layer in a neural network (Xu *et al.* 2020, Cai *et al.* 2021). The neural network employs interlinked neurons to model the functional relationships between inputs and outputs. The equation below represents each neuron which is seen as a calculation cell

$$y = \max(0, \sum_i w_i x_i + b) \quad (1)$$

where y and x_i represent values of output and input in each neuron; w_i is connection weight; b denotes bias value.

The Eqs. (2) and (3) below build a mapping between inputs and outputs

$$h_i = \max(0, W_i \cdot h_{i-1} + b_i) \text{ for } 1 \le i \le L, \text{and } h_0 = x \quad (2)$$

$$y = \max(0, V \cdot h_L) \quad (3)$$

where L represents the layer numbers; matrices $W_1, \dots W_L, V$, and vectors $b_1, \dots b_L$ are model parameters got from the dataset.

Each network is comprised of an input layer, an output layer, and a few hidden layers. As mentioned above, the number of hidden layers and number of neurons in each

hidden layer are two major hyperparameters of ANN in this study. Owing to the significant influence of ANN configuration on prediction accuracy, seeking the optimal hyperparameters of ANN is essential. Thereby, this study adopts the PSO algorithm to automatically search the optimal hyperparameters. After determining the model configuration, the output of the former layer gives value to the input of the latter one. Fig. 4(a) presents a classic ANN framework. It is named the feed-forward type of network because the computation only goes on along the direction forward. In the output layer, the following active function was used mainly due to its superior performance (Zhang *et al.* 2020)

$$\mathrm{f(x)} = \frac{2}{1+\exp(-\mathrm{x})} - 1 \tag{4}$$

Back propagation (BP) is a training procedure for ANN optimisation and its operation mode is schematically presented in Fig. 4(b). Errors between predicted and calculated output values are computed by the network in each operation. These errors are propagated backward in several iterations. The iteration and adjustment of their weights are conducted and the mean square error (MSE) between expected and observed outputs is effectively reduced in this process (Zhang and Wang 2019, Shi *et al.* 2020). In the steepest gradient descent principle employed here, weights are updated according to the error gradient directly, i.e.

$$\Delta w_n = \alpha \Delta w_{n-1} - \eta \frac{\partial E}{\partial w} \tag{5}$$

where w means the weight between two neurons; Δw_n and Δw_{n-1} represent the variation according to the weight when it iterates n and $n-1$ times; α and η are the momentum factor and learning rate.

The final connection weights are fixed upon finishing the training procedure. Moreover, new input modes will be attained by the network to produce corresponding output and mapping. Among all these parameters, the connection weights, bias values, the amount of hidden layers and neurons in each layer directly influence the function of BPNN which will be tuned by PSO.

3.2 Baseline models

The PSO-BPNN model was compared with LR and MLR to evaluate their forecast ability. The LR model with several predictive variables is shown in Eq. (5) (Hosmer Jr *et al.* 2013).

$$ln\frac{p}{1-p} = b_0 + \sum_{k=1}^{n} b_k x_k \tag{6}$$

where x_k is an independent and p is a dependent variate; b_0 and b_k are constant coefficients. Eq. (6) presents the relationship between the output variable Y and multiple predictive variables x_n in the MLR model (Nathans *et al.* 2012, Sun *et al.* 2019).

$$Y = \beta_0 + \beta_1 x_1 + \beta_1 x_2 + \cdots + \beta_n x_n \tag{7}$$

where $\beta_1, \ldots, \beta_n$ denote the regression coefficients.

3.3 Particle swarm optimization

Hyperparameters of BPNN are adjusted by PSO which is a global optimisation algorithm. One particle within the searching scope represents one possible candidate solution in PSO. Specifically, the above-mentioned two hyperparameters are assumed as the particles of the PSO algorithm. According to the PSO algorithm, the number of hidden layers will be set as 1, 2, and 3, respectively. Then, the number of neurons in each hidden layer will be tuned within limited iterations (50 in this study), aiming at achieving the minimum root-mean-square error (RMSE) value on the validation set (section 3.4). It is noted that the empirical scope of the number of neurons in each hidden layer is ranging from 1 to 20 and the initial value is set as 10 in this study. During the tuning process, a particle's orientation is optimised based on its preceding best position and the present best position of the rest of the swarm which can be translated into

$$v_{id}^{t+1} = w \times v_{id}^{t} + C_1 \times r_{1i} \times (pbest_{id} - x_{id}^{t}) + C_2 \times r_{2i} \times (gbest_{id} - x_{id}^{t}) \tag{8}$$

$$x_{id}^{t+1} = x_{id}^{t} + v_{id}^{t+1} \tag{9}$$

where d means the dimension of the searching scope; v_{id}^{t} and v_{id}^{t+1} are the velocities of particle *i* when it iterates *t* and *t+1* times; x_{id}^{t} and x_{id}^{t+1} are the coordinates of particle *i* when it iterates *t* and *t+1* times; $pbest_{id}$ and $gbest_{id}$ are the best given location of the particle and the best given location of the whole swarm; w represents the original weights; C_1 and C_2 are acceleration factors (the value is usually 2); r_{1i} and r_{2i} are two values picked from 0 to 1 randomly.

It is noted that PSO fails to provide the highest prediction accuracy if the program is carried out for only one time owing to its inherent stochastic properties. Several run times are conducted and the statistical outcomes are compared to verify the feasibility of the proposed procedure. In this paper, the results of only one run time are presented.

3.4 Cross validation and performance evaluation measure

Small data sets leading to overfitting problems is a common issue that could be solved by employing 10-fold cross-validation (CV) (Cawley and Talbot 2010, Alam *et al.* 2020). Specifically, the hyperparameters are adjusted on a randomly segmented training set (the external training set) comprising seventy percent of the samples (Hsu *et al.* 2003). Moreover, the external training set is segmented into a validation set (comprising ten percent of the external training data) and an internal training set (comprising ninety percent of the external training data). PSO seeks optimum BPNN hyperparameters on the internal training set. It also computes the RMSE of the validation set to assess the characteristics of the model. This procedure is duplicated ten times to attain ten RMSE values. Model

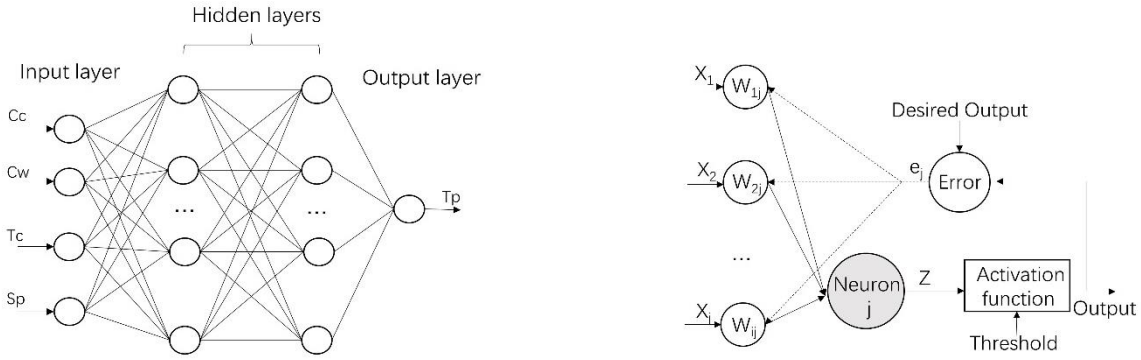

(a) T=60°C (b) T=80°C

Fig. 4 Architecture of neural networks

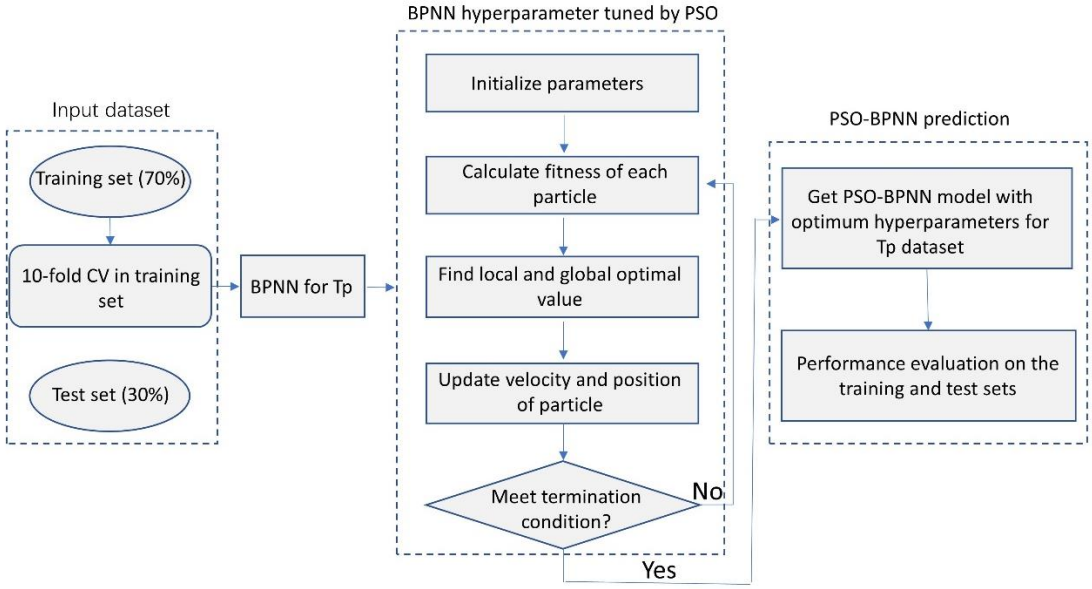

Fig. 5 BPNN model training tuned by PSO

hyperparameters with the minimum RMSE values are the prime ones and will be chosen to configurate the ANN model. The procedure of BPNN model training by 10-fold CV and PSO is shown in Fig. 5.

In this research, the root mean square error, correlation coefficient (R), mean absolute error (MAE), and mean absolute percentage error (MAPE) employed to assess the ML models' characteristics are defined as

$$RMSE = \sqrt{\frac{1}{N}\sum_{i=1}^{N}(y_i^* - y_i)^2} \tag{10}$$

$$R = \frac{\Sigma_{i-1}^{N}(y_i^* - \overline{y^*})(y_i - \bar{y})}{\sqrt{\Sigma_{i=1}^{N}(y_i^* - \overline{y^*})^2}\sqrt{\Sigma_{i=1}^{N}(y_i - \bar{y})^2}} \tag{11}$$

$$MAPE = \frac{1}{N}\sum_{i=1}^{n}\left|\frac{y_i^* - y_i}{y_i}\right| \tag{12}$$

$$MAE = \frac{1}{N}\sum_{i=1}^{n}|y_i^* - y_i| \tag{13}$$

where N means the number of samples in the dataset; y_i^* denotes the forecasted output of ML models; y_i denotes the real output in the dataset; $\overline{y^*}$ represents the forecasted mean value, and $\bar{y}$ represents the real mean value in the dataset.

4. Results and discussion

4.1 Results of the pullout test

Fig. 6 presents the ultimate interface bond strengths of 7, 14, and 28-day with varying cement and water contents. The ultimate strength was positively correlated to C_c. As C_c increased from 6% to 30%, the bond strength improved approximately 54 times, reaching 3879.40 kPa (C_w =50%,

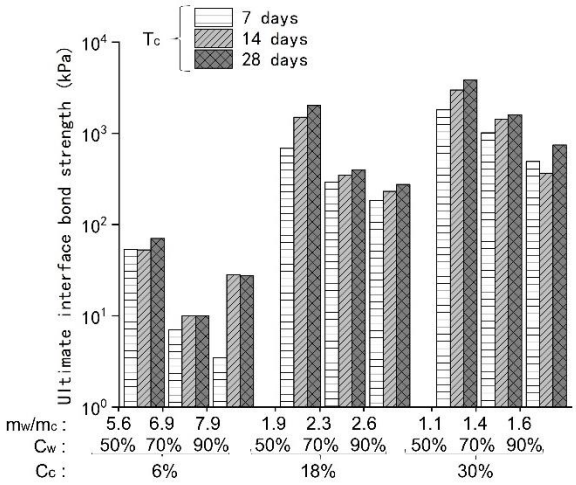

Fig. 6 Ultimate interface bond strength of the pullout specimens

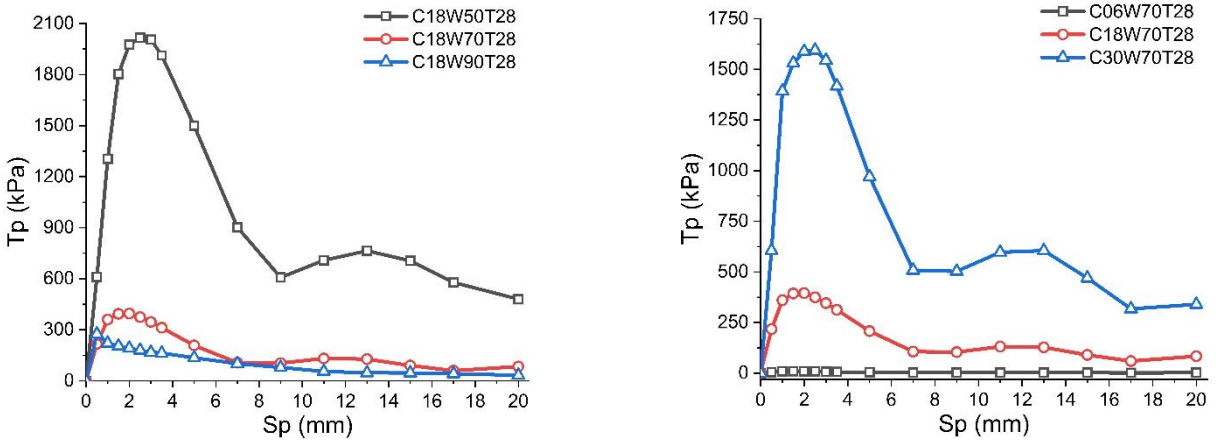

(a) Curves for specimens (varying C_w and 18% C_c) (b) Curves for specimens (varying C_c and 70% C_w)

Fig. 7 Bond-slip curves for different specimens at 28 curing days

T_C =28 days). This was attributed to higher cement content resulting in more hydraulic reactions and consequently increased cementitious products generated within the cement-soil matrix. But upon water content raising to 90%, the strength only increased 26 times, reaching 745.30 kPa. That is, water content negatively affected the ultimate bonding performance. In addition, when C_c was 30% and T_C was 28 days, the strength decreased by approximately 81%, from 3879.40 to 745.30 kPa, as C_w rose from 50% to 90%. This reduction was due to extra water leading to insufficient hydration reaction. However, the strength only decreased by 61% when C_c is 6%. These phenomena could be concluded that both C_w and C_c had a stronger influence on the ultimate strength when the water-cement ratio was low. This was ascribed to the fact that extra water led to pore pressure in the curing time which resulted in a porous interface microstructure (Å hnberg 2006, Zhang 2014).

The 28-day bond-slip curves of specimens with varying C_w and C_s are presented in Fig. 7. Due to the existence of the ribs, tendons and cemented soil were interlocked tightly so that their relative motion was constrained with each other. Thereby, the elastic stage (the positive proportion between T_p and S_p) was initially obtained when tendons started to move (Wu *et al.* 2019, Abedini and Zhang 2021, Zhang *et al.* 2022). Besides, the initial plastic zones and shear failure surfaces were shaped and extended during this stage. The elasticity and corresponding ultimate strength were negatively affected by the water content. The 2.5 mm slip distance and 2016 kPa peak strength were obtained for sample C18W50T28. However, the values were decreased to 0.5 mm and 275 kPa, respectively when the water content increased to 90% (C18W90T28). This was attributed to extra water leading to the formation of pores inside the cemented soil and insufficient cementitious products generated. It weakened the cement stabilization and consequently increased the level of the soil fragments' detachment and lowered the shear capacity of the cemented soil matrix. Similarly, the increase of cement content enhanced the elasticity and ultimate strength of GFRTS, which was presented in Fig. 7(b).

The T_p was gradually reduced to residual strength (the first trough) when the slip distance increased to around 9 mm. During this process, the soil fragments were gradually detached to fill the space between the ribs, reducing the effective rib height, diminished interlock effect, and consequently lowered T_p. The residual strength was affected

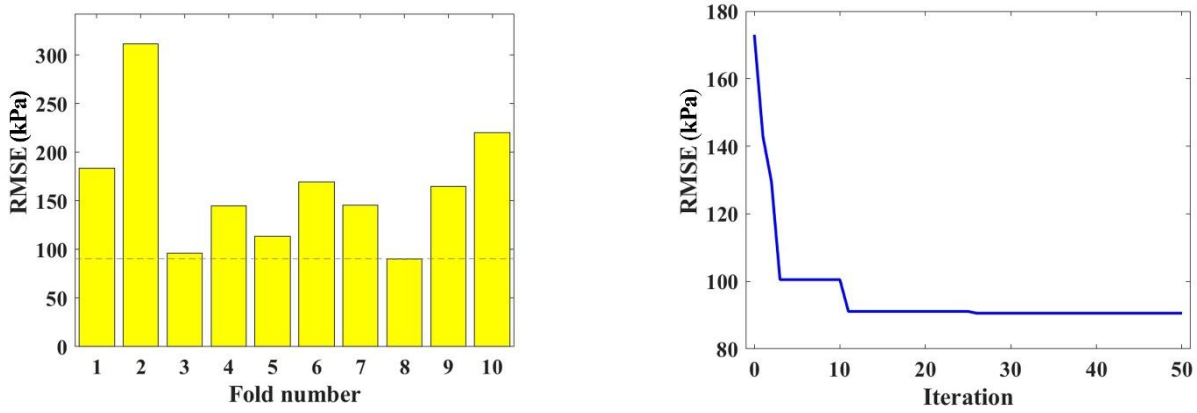

(a) RSME values from 10 validation sets (b) RSME convergency at the 26th iteration

Fig. 8 Hyperparameters tuning for FS prediction

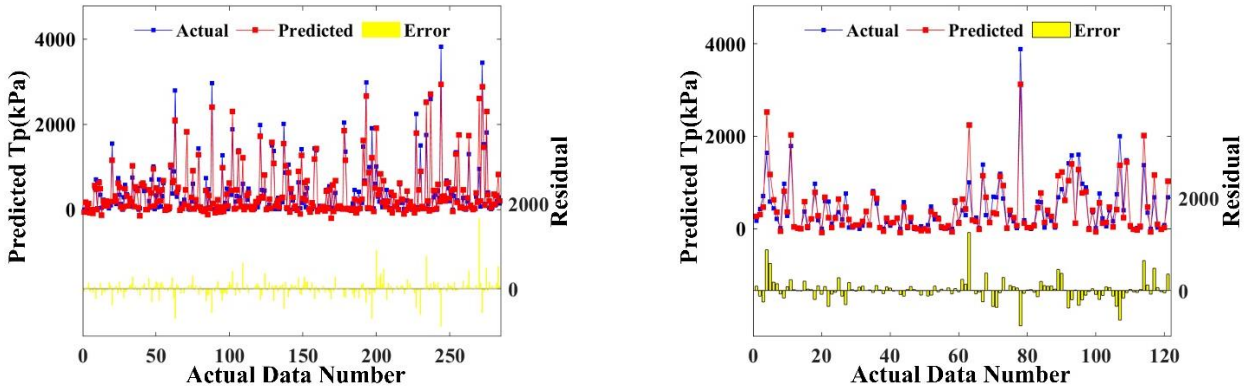

(a) Training set (b) Test set

Fig. 9 Difference between forecasted and measured T_p

positively by C_c and negatively by C_w. As C_c grown from 6% to 30%, the residual strength increased from 2.63 kPa to 502.89 kPa (C_w =70%, T_c=28 days). Nevertheless, it witnessed a reduction from 607.44 kPa to 32.83 kPa as C_w grew from 50% to 90% (C_c =18%, T_c=28 days). In addition, the second peak strength (at approximately 13 mm slip distance) appeared in samples with cement content over 18% or water content under 70%. This phenomenon was due to the regenerated smaller plastic zones and shear failure surfaces because of the reduced rib height (Chen *et al.* 2020). It further verified the effectiveness of a high cement-water ratio on the cemented soil's robustness. In conclusion, samples with high C_c or low C_w possessed enhanced elasticity, ultimate strength, and residual bond strength, which were all positively affected by cement content and negatively influenced by water content.

4.2 Modelling results for Tp

4.2.1 Hyperparameter tuning

The BPNN with the optimum hyperparameters is picked from the 8th fold with the smallest RMSE employing PSO and 10-fold CV, as illustrated in Fig. 8(a). Fig. 8(b) presents the RMSE convergency and hyperparameters adjusting by PSO. It shows that the RMSE reached a minimum at the 26th iteration in the 8th fold and stayed constant at the remaining iterations. The attained optimal BPNN framework comprises a hidden layer with 10 neurons. co Moreover, in the 70% training dataset, the bias values and connection weights of BPNN with constant framework were adjusted by PSO. Eventually, the adjusted BPNN model with a 3-10-1 framework (3 neurons in the input layer; 10 in the hidden layer; 1 in the output layer) was employed to forecast bond strength.

4.2.2 Performance of PSO-BPNN for Tp modeling

Fig. 9 presents the comparison of forecasted and real T_p for testing and training datasets with the optimal BPNN. Minor errors were found in both sets, thereby such PSO-BPNN model was dependable to assess T_p. Besides, computed correlation coefficients were applied to evaluate the relationship between the forecasted and measured T_p outcome, as presented in Fig. 10. The coefficients were 0.9402 and 0.9080 for training and test sets respectively displaying that this model is reliable again. Moreover, the RMSE/R value for both sets was near proving that the fitting was moderate without overfitting problems.

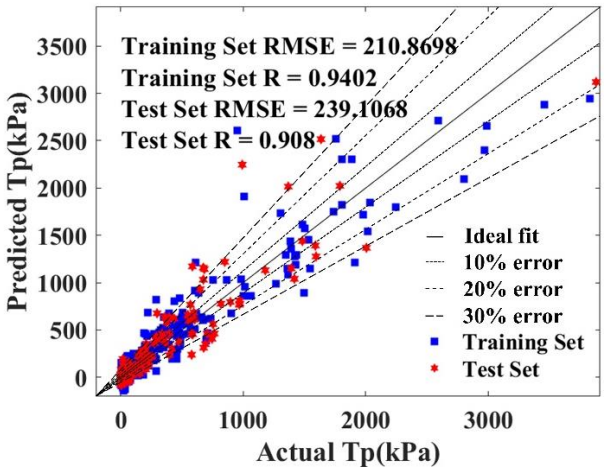

Fig. 10 Scatter plot of simulated and actual FS for training and test sets

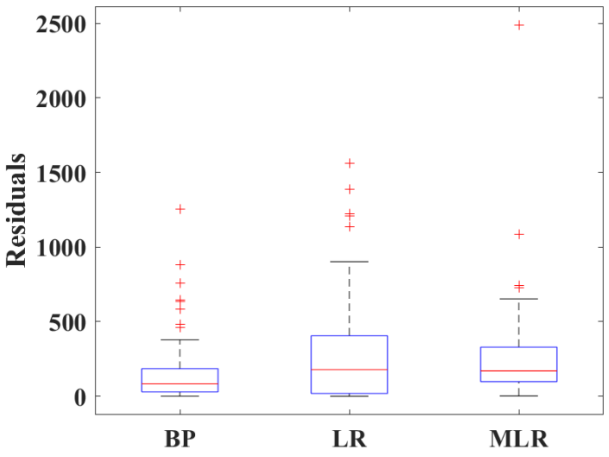

(a)

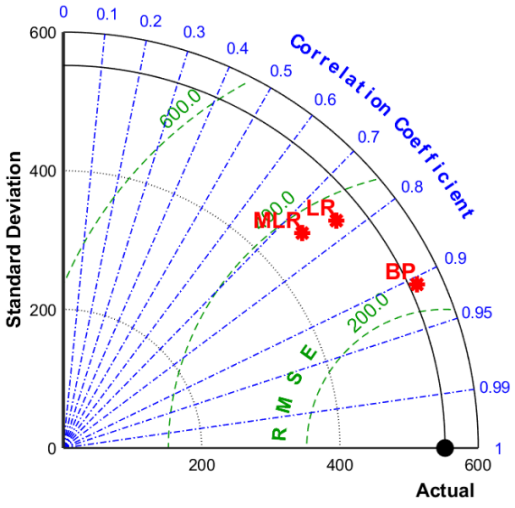

(b)

Fig. 11 Performance evaluation of three models by (a) Boxplot and (b) Taylor diagram

Furthermore, the comparison of forecasting ability between the PSO-BPNN model and benchmark models including MLR and LR was conducted in this research. The diversity between the results of forecasted and laboratorial

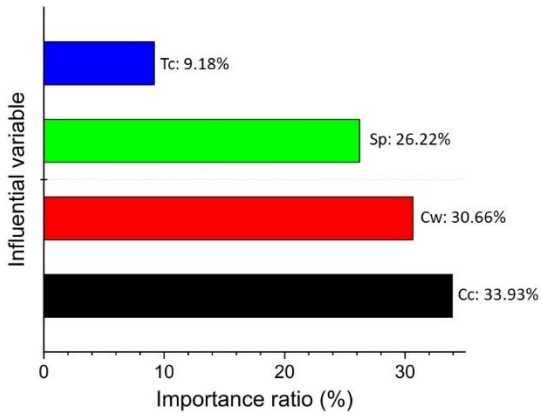

Fig. 12 The relative importance of each variable on T_p of GTRCS

Table 4 Evaluation of three ML models on the bond strength test set

Evaluation index	Model		
	BPNN	LR	MLR
RMSE (kPa)	239.11	402.00	370.83
R	0.9080	0.7692	0.7449

T_p employs a box plot for MLR, R, and BPNN as shown in Fig. 11(a). The BPNN model had the smallest median value (the red line) and the narrowest interquartile range (the space between the top and bottom blue lines) compared to the other two. It represented that this model had the lowest prediction error among all three models. In addition, the high excellence of BPNN in forecasting T_p was also illustrated by the lowest upper limit (the black line), although several outliers existed. Moreover, the integration of three indices in model evaluation (RMSE, R, and standard deviation) using polar coordinates is presented in Fig. 13(b). Similarly, the BPNN model performed the best again for it was the nearest to the "actual" point in the Taylor diagram. It has the smallest RMSE, the largest R value, and minimum standard deviation values among all three models. Various forecasting models' operation statistics in the testing set are listed in Table 3. These comparison consequences denote that using the PSO-BPNN model is an optimal method to forecast the T_p of GTRCS.

4.3 Variable significance for bond strength

Fig. 12 presents the significance ranking of affecting variables employing SA. The significance score of cement content was 33.93%, making it the most significant affecting variable, higher than that of water content and slip distance which was 30.66% and 26.22%, respectively. The discovery mentioned above that T_p development was extremely susceptible to C_c and C_w was consistent with such ranking (Singh *et al.* 2011, Tsai *et al.* 2019). Moreover, the significance score of curing time was only 9.18%, namely the lowest one. Consequently, this significance metric quantitatively analyses these input variables which offers an outstanding way to comprehend the development of T_p.

5. Conclusions

In this study, the interface bond performance between the cemented soil matrix and GFRP tendons was investigated by conducting pullout tests. Based on the testing results, a PSO-BPNN model was trained to predict the bond strength and the forecasted values were consistent with the generated results. The concluding remarks were depicted as follows.

- The ultimate interface bond strength was positively influenced by cement content and negatively by water content. Sample C30W50T28 showed the largest ultimate strength which was 3879.40 kPa. Besides, high cement to water ratio enhanced the robustness of GTRCS to withstand detachment of soil matrix which led to increased elasticity and residual strength.
- The PSO-BPNN model was built in a framework where there were 3 neurons in the input layer, 10 in the hidden layer, and 1 in the output layer. Its RMSE reached a minimum value at the 26^{th} iteration in the 8^{th} fold. The accuracy of the PSO-BPNN model in forecasting bond strength was reflected in a lower RMSE (239.11 kPa) and higher R (0.9080) compared with MLR and LR. Besides, its correlation coefficients were 0.9402 and 0.9080 for training and test sets respectively, displaying its reliability.
- The significance ranking of variables showed that cement content was the most significant followed by water content and slip distance, and curing time was of the least significance. The results also complied with the experimental findings.

For limited statistics will strongly affect the forecast capacity of PSO-BPNN models, a larger database is needed in the successive research. Moreover, the exploration of more variables is essential such as the tendon type, soil components, etc. Other progressive or evolved AI technologies should also be applied to enhance usability, efficiency, and correctness.

Acknowledgements

The research described in this paper was financially supported by the National Natural Science Foundation of China (grant numbers 51908201 and 51978254), Natural Science Foundation of Hunan Province (grant number 2020JJ5024), and the Key R&D Project of Hunan Province Intelligent Disaster Prevention and Mitigation and Ecological Restoration in Civil Engineering (grant number 2020SK2109). Meanwhile, this work was supported by Hunan Key Laboratory of Intelligent Disaster Prevention and Mitigation and Ecological Restoration in Civil Engineering, Hunan Provincial Engineering Research Center, Catastrophe and Reinforcement of Dangerous Engineering Structures. This research was also supported by Academic Research Council of Australia Linkage Projects for Asset Intelligence: Maximising Operational Effectiveness for Digital Era (Grant No. LP180100222).

References

Abedini, M. and C. Zhang (2021), "Dynamic performance of concrete columns retrofitted with FRP using segment pressure technique", *Compos. Struct.*, **260**, 113473. https://doi.org/10.1016/j.compstruct.2020.113473.

Abedini, M. and Zhang, C. (2021), "Dynamic vulnerability assessment and damage prediction of RC columns subjected to severe impulsive loading", *Struct. Eng. Mech.*, **77**(4), 441-461. https://doi.org/10.12989/sem.2021.77.4.441.

Abedini, M., Zhang, C., Mehrmashhadi, J. and Akhlaghi, E (2020), "Comparison of ALE, LBE and pressure time history methods to evaluate extreme loading effects in RC column", *Structures*, **28**, 456-466. https://doi.org/10.1016/j.istruc.2020.08.084.

Abido, M.A. (2002), "Optimal power flow using particle swarm optimizatio", *Int. J. Elec. Power & Energy Syst.*, **24**(7), 563-571. https://doi.org/10.1016/S0142-0615(01)00067-9.

Åhnberg, H. (2006), *Strength of Stabilised Soil-A Laboratory Study on Clays and Organic Soils Stabilised with different Types of Binder*. Avd. för Byggnadsmekanik / Department of Construction Sciences, LTH, Lund, Sweden.

Alam, Z., Sun, L., Zhang, C., Su, Z. and Samali, B. (2020), "Experimental and numerical investigation on the complex behaviour of the localised seismic response in a multi-storey plan-asymmetric structure", *Struct. Infrastruct. Eng.*, **17**(1), 86-102. https://doi.org/10.1080/15732479.2020.1730914.

Alam, Z., Zhang, C. and Samali, B. (2020), "Influence of seismic incident angle on response uncertainty and structural performance of tall asymmetric structure", *Struct. Des. Tall Spec. Build.*, **29**(12), e1750. https://doi.org/10.1002/tal.1750

Alam, Z., Zhang, C. and Samali, B. (2020), "The role of viscoelastic damping on retrofitting seismic performance of asymmetric reinforced concrete structures", *Earthq. Eng. Eng. Vib.*, **19**(1), 223-237. https://doi.org/10.1007/s11803-020-0558-x.

Babasaki, R. (1996), "Japanese Geotechnical Society technical committee report-Factors influencing the strength of improved soil", *Proceedings of the 2nd Int. Conf. Ground Improvement Geosystems-Grouting and Deep Mixing-*, Tokyo, Japan, May.

Cai, K., Chen, H., Ai, W., Miao, X., Lin, Q. and Feng, Q. (2021), "Feedback convolutional network for intelligent data fusion based on near-infrared collaborative IoT technology", *IEEE T. Ind. Inform.*, **17,** 1123-1135. https://doi.org/10.1109/TII.2021.3076513.

Cawley, G.C. and Talbot, N. L. (2010), "On over-fitting in model selection and subsequent selection bias in performance evaluation", *J. Machine Learning Research*, **11**(1), 2079-2107. https://dl.acm.org/doi/10.5555/1756006.1859921.

CECS147, C. (2016), Technical specification for soil mass with reinforced cement soil pile and anchors, China Planning Press, Beijing, China.

Chandwani, V., Agrawal, V., Nagar, R. and Signh, S. (2015), "Modeling slump of ready mix concrete using genetic algorithms assisted training of Artificial Neural Networks", *Int. J. Technol.*, **42**(2), 885-893. https://doi.org/10.1016/j.eswa.2014.08.048.

Chen, C., Zhang, G., Zornberg, J. G., Morsy, A. M., & Huang, J. (2020), "Interface bond behavior of tensioned glass fiber-reinforced polymer (GFRP) tendons embedded in cemented soils", *Construction and Building Materials*, **263**, 120-132. https://doi.org/10.1016/j.conbuildmat.2020.120132

Chen, C., Zhang, G., Zornberg, J.G., Morsy, A.M., Zhu, S. and Zhao, H. (2018), "Interface behavior of tensioned bars embedded in cement-soil mixtures", *Constr. Build. Mater.*, **186**, 840-853. https://doi.org/10.1016/j.conbuildmat.2018.07.211.

Chew, S.H., Kamruzzaman, A.H.M. and Lee, F.H. (2004), "Physicochemical and engineering behavior of cement treated clays", *J. Geotech. Geoenviron. Eng.*, **130**(7), 696-706.

https://ascelibrary.org/doi/abs/10.1061/(ASCE)10900241(2004)130:7(696).

Fan, P., Deng, R., Qiu, J., Zhao, Z.. and Wu, S. (2021), "Well logging curve reconstruction based on kernel ridge regression", *Arabian J. Geosci.*, **14**(16), 1-10. https://doi.org/10.1007/s12517-021-07792-y.

Feng, W., Wang, Y., Sun, J., Tang, Y., Wu, D., Jiang, Z., Wang, J. and Wang, X. (2021), "Prediction of thermo-mechanical properties of rubber-modified recycled aggregate concrete", ., **318**, 125970. https://doi.org/10.1016/j.conbuildmat.2021.125970.

Fernández-Martínez, J. and Fernández-Muñiz, Z. (2020), "The curse of dimensionality in inverse problems", *J. Comput. Appl. Math.*, **369**, 112571. https://doi.org/10.1016/j.cam.2019.112571.

Gholipour, G., Zhang, C. and Mousavi, A. A. (2020), "Nonlinear numerical analysis and progressive damage assessment of a cable-stayed bridge pier subjected to ship collision", *Mar. Struct.*, **69**, 102662. https://doi.org/10.1016/j.marstruc.2019.102662.

Han, J. (2014), *Principles and Practice of Ground Improvement*, John Wiley & Sons, Inc., Hoboken, New Jersey, United States.

Horpibulsuk, S., Miura, N. and Nagaraj, T.S. (2003), "Assessment of strength development in cement-admixed high water content clays with Abrams' law as a basis", *Geotechnique*, **53**(4), 439-444. https://doi.org/10.1680/geot.2003.53.4.439.

Hosmer Jr, D.W., Lemeshow, S. and Sturdivant, R.X. (2013), *Applied logistic regression*, John Wiley & Sons, Inc., Hoboken, New Jersey, United States.

Hou, L., Wu, S., Zhang, G., Tan, Y. and Wang, X. (2021), "Literature review of digital twins applications in construction workforce safety", *Appl. Sci.*, **11**(1), 339. https://doi.org/10.3390/app11010339.

Hsu, C.W., Chang, C.C. and Lin, C.J. (2003), "A practical guide to support vector classification", Technical report, Department of Computer Science, National Taiwan University.

Ju, Y., Shen, T. and Wang, D. (2020), "Bonding behavior between reactive powder concrete and normal strength concrete", *Constr. Build. Mater.*, **242**, 118024 https://doi.org/118010.111016/j.conbuildmat.112020.118024.

Kitazume, M. and Terashi, M. (2013), *The Deep Mixing Method*, CRC Press/Balkeman, Leiden, Netherlands.

Li, J., Qin, Q., Sun, J., Ma, Y. and Li, Q. (2020), "Mechanical and conductive performance of electrically conductive cementitious composite using graphite, steel slag, and GGBS", *Struct. Concrete*, early view. https://doi.org/10.1002/suco.202000617

Liu, J., Wu, C., Wu, G. and Wang, X. (2015), "A novel differential search algorithm and applications for structure design", *Appl. Math. Comput.*, **268**, 246-269. https://doi.org/10.1016/j.amc.2015.06.036.

Luo, J., Li, M., Liu, X., Tian, W., Zhong, S. and Shi, K. (2020), "Stabilization analysis for fuzzy systems with a switched sampled-data control", *J. Franklin Inst.*, **357**(1), 39-58. https://doi.org/10.1016/j.jfranklin.2019.09.029.

Medvedeva, M.A., Simos, T.E. and Tsitouras, C. (2020), "Variable step-size implementation of sixth-order Numerov-type methods", *Math. Method. Appl. Sci.*, **43**(3), 1204-1215. https://doi.org/10.1002/mma.5929.

Mou, B. and Bai, Y. (2002), "Experimental investigation on shear behavior of steel beam-to-CFST column connections with irregular panel zone", *Eng. Struct.*, **168**, 487-504. https://doi.org/10.1016/j.engstruct.2018.04.029.

Nathans, L.L., Oswald, F.L. and Nimon, K. (2012), "Interpreting multiple linear regression: A guidebook of variable importance", *Pract. Assessment, Res. Eval.*, **17**(9), 1-19. https://doi.org/10.7275/5fex-b874.

Qin, C., Tao, J., Shi, H., Xiao, D., Li, B. and Liu, C. (2020), "A novel Chebyshev-wavelet-based approach for accurate and fast prediction of milling stability", *Precision Eng.*, **62**, 244-255. https://doi.org/10.1016/j.precisioneng.2019.11.016.

Shen, S.L., Wang, Z.F., Yang, J. and Ho, C.E. (2013), "Generalized approach for prediction of jet grout column diameter", *J. Geotech. Geoenviron. Eng.*, **139**(12), 2060-2069. https://ascelibrary.org/doi/full/10.1061/%28ASCE%29GT.1943-5606.0000932.

Shi, J., Lu, Y. and Zhang, J. (2020), "Approximation Attacks on Strong PUFs", *IEEE T. Comput.-Aided Des. Integrated Circuit. Syst.*, **39**(10), 2138-2151. https://doi.org/10.1109/TCAD.2019.2962115.

Singh, V., Gu, N. and Wang, X. (2011), "A theoretical framework of a BIM-based multi-disciplinary collaboration platform", *Autom. Constr.*, **20**(2), 134-144. https://doi.org/10.1016/j.autcon.2010.09.011.

Sun, J., Ma, Y., Li, J., Zhang, J., Ren, Z. and Wang, X. (2021), "Machine learning-aided design and prediction of cementitious composites containing graphite and slag powder", *J. Build. Eng.*, **43**, 102544. https://doi.org/10.1016/j.jobe.2021.102544.

Sun, J., Wang, X., Zhang, J., Xiao, F., Sun, Y., Ren, Z., Zhang, G., Liu, S. and Wang, Y. (2021), "Multi-objective optimisation of a graphite-slag conductive composite applying a BAS-SVR based model", *J. Build. Eng.*, **44**, 103223. https://doi.org/10.1016/j.jobe.2021.103223.

Sun, J., Wang, Y., Yao, X., Ren, Z., Zhang, G., Zhang, C., Chen, X., Ma, W. and Wang, X. (2021), "Machine-learning-aided prediction of flexural strength and ASR expansion for waste glass cementitious composite", *Appl. Sci.*, **11**(15), 6686. https://doi.org/10.3390/app11156686.

Sun, Y., Li, G., Zhang, J., Sun, J. and Xu, J. (2020), "Development of an ensemble intelligent model for assessing the strength of cemented paste backfill", *Adv. Civil Eng.*, **2020**, 1-6. https://doi.org/10.1155/2020/1643529.

Sun, Y., Zhang, J., Li, G., Ma, G., Huang, Y., Sun, J. and Nener, B. (2019), "Determination of Young's modulus of jet grouted coalcretes using an intelligent model", *Eng. Geol.*, **252**, 43-53. https://doi.org/10.1016/j.enggeo.2019.02.021.

Sun, Y., Zhang, J., Li, G., Wang, Y., Sun, J. and Jiang, C. (2019), "Optimized neural network using beetle antennae search for predicting the unconfined compressive strength of jet grouting coalcretes", *Int. J. Numer. Anal. Method. Geomech.*, **43**(4), 801-813. https://doi.org/10.1002/nag.2891.

Tepfers, R., *et al*. (2000), *Bond of reinforcement in concrete*, International Federation for Structural Concrete (fib), Lausanne, Switzerland.

Timoney, M.J. and McCabe, B.A. (2017), "Strength verification of stabilised soil-cement columns: A laboratory investigation of the Push-In Resistance Test (PIRT)", *Can. Geotech. J.*, **54**(6), 789-805. https://doi.org/10.1139/cgj-2016-0230.

Timoney, M.J., McCabe, B.A. and Bell, A.L. (2012), "Experiences of dry soil mixing in highly organic soils", *Proceedings of the Institution of Civil Engineers-Ground Improvement*, **165**(1), 3-14. https://doi.org/10.1680/grim.2012.165.1.3.

Tsai, Y.H., Wang, J., Chien, W.T., Wei, C.Y., Wang, X. and Hsieh, S.H. (2019), "A BIM-based approach for predicting corrosion under insulation", *Automat. Constr.*, **107**, 102923. https://doi.org/10.1016/j.autcon.2019.102923.

Wang, J., Dai, Q. and Si, R. (2022), "Experimental and numerical investigation of fracture behaviors of steel fiber–reinforced rubber self-compacting concrete", *J. Mater.Civil Eng.*, **34**(1), 04021379. https://doi.org/10.1061/(ASCE)MT.1943-5533.0004010.

Wang, J., Dai, Q., Si, R. and Guo, S. (2018), "Investigation of properties and performances of Polyvinyl Alcohol (PVA) fiber-

reinforced rubber concrete", *Constr. Build. Mater.*, **193**, 631-642. https://doi.org/10.1016/j.conbuildmat.2018.11.002.

Wang, L., Yuan, J., Wu, C. and Wang, X. (2019), "Practical algorithm for stochastic optimal control problem about microbial fermentation in batch culture", *Optim. Lett.*, **13**(3), 527-541. https://doi.org/10.1007/s11590-017-1220-z.

Wang, L., Peng, Y., Xie, Y., Chen, B. and Du,Y. (2021), "A new iteration regularization method for dynamic load identification of stochastic structures", *Mech. Syst. Signal Pr.*, **156**, 107586. https://doi.org/10.1016/j.ymssp.2020.107586.

Wu, C., Wang, X., Chen, M. and Kim, M.J. (2019), "Differential received signal strength based RFID positioning for construction equipment tracking", *Adv. Eng. Inform.*, **42**, 100960. https://doi.org/10.1016/j.aei.2019.100960.

Xie, W., Zhang, R., Zeng, D., Shi, K. and Zhong, S. (2020), "Strictly dissipative stabilization of multiple-memory Markov jump systems with general transition rates: A novel event-triggered control strategy", *Int. J. Robust Nonlinear Control*, **30**(5), 1956-1978. https://doi.org/10.1002/rnc.4856.

Xu, D., Liu, Q., Qin,Y. and Chen, B. (2020), "Analytical approach for crack identification of glass fiber reinforced polymer–sea sand concrete composite structures based on strain dissipations", *Struct. Health Monit.*, **19**(2), 1475921720974290. https://doi.org/10.1177/1475921720974290.

Xu, D.S., Huang, M. and Zhou, Y. (2020), "One-dimensional compression behavior of calcareous sand and marine clay mixtures", *Int. J. Geomech.*, **20**(9), 04020137. https://doi.org/10.1061/(ASCE)GM.1943-5622.0001763.

Xu, S., Wang, J., Shou, W., Ngo, T. and Wang, X. (2021), "Computer vision techniques in construction: a critical review", *Arch. Comput. Method. Eng.*, **28**, 3383-3397. https://doi.org/10.1007/s11831-020-09504-3.

Yan, F. and Lin, Z. (2016), "Bond behavior of GFRP bar-concrete interface: damage evolution assessment and FE simulation implementations", *Compos. Struct.*, **155**, 63-76. https://doi.org/10.1016/j.compstruct.2016.07.078.

Zhang, C. (2014), "Control Force Characteristics of Different Control Strategies for the Wind-Excited 76-Story Benchmark Building Structure", *Advances in Structural Engineering*, **17**(4), 543-559. https://doi.org/10.1260/1369-4332.17.4.543

Zhang, C. and H. Wang (2019), "Robustness of the active rotary inertia driver system for structural swing vibration control subjected to multi-type hazard excitations", *Appl. Sci.*, **9**(20), 4391. https://doi.org/10.3390/app9204391.

Zhang, G., Chen, C., Li, K., Xiao, F., Sun, J., Wang, Y. and Wang, X. (2022), "Multi-objective optimisation design for GFRP tendon reinforced cemented soil", *Constr. Build. Mater.*, **320**, 126297. https://doi.org/10.1016/j.conbuildmat.2021.126297.

Zhang, J., Huang, Y., Wang, Y. and Ma, G. (2020), "Multi-objective optimization of concrete mixture proportions using machine learning and metaheuristic algorithms", *Constr. Build. Mater.*, **253**, 119208. https://doi.org/10.1016/j.conbuildmat.2020.119208.

Zhang, J., Sun, Y., Li, G., Wang, Y., Sun, J. and Li, J. (2020), "Machine-learning-assisted shear strength prediction of reinforced concrete beams with and without stirrups", *Eng. with Comput.*, 1-15. https://doi.org/10.1007/s00366-020-01076-x.

Zhang, W., Li, H., Li, Y., Liu, H., Chen, Y. and Ding, X. (2021), "Application of deep learning algorithms in geotechnical engineering: a short critical review", *Artif. Intell. Rev.*, **54**, 5633-5673. https://doi.org/10.1007/s10462-021-09967-1.

Zhang, W., Wu, C., Zhong, H., Li, Y. and Wang, L. (2021), "Prediction of undrained shear strength using extreme gradient boosting and random forest based on Bayesian optimization", *Geosci. Frontiers*, **12**(1), 469-477. https://doi.org/10.1016/j.gsf.2020.03.007.

Zhao, C., Zhong, S., Zhang, X., Zhong, Q.a and Shi, K. (2020), "Novel results on nonfragile sampled-data exponential synchronization for delayed complex dynamical networks", *Int. J. Robust Nonlinear Control*, **30**(10), 4022–4042. https://doi.org/10.1002/rnc.4975.

Zhao, R., Zhang, L., Guo, B., Chen, Y., Fan, G., Jin, Z., Guan, X., and Zhu, J. (2021), "Unveiling substitution preference of chromium ions in sulphoaluminate cement clinker phases", *Compos. Part B: Eng.*, **222**(14), 109092. https://doi.org/10.1016/j.compositesb.2021.109092.

Zheng, J., Zhang, C. and Li, A. (2020), "Experimental investigation on the mechanical properties of curved metallic plate dampers", *Appl. Sci.*, **10**(1), 269. https://doi.org/10.3390/app10010269.

Zhu, J., Yang, K., Chen, Y., Fan, G., Zhang, L., Guo, B. and Zhao, R. (2021), "Revealing the substitution preference of zinc in ordinary Portland cement clinker phases: A study from experiments and DFT calculations", *J. Hazard. Mater.*, **409**, 124504. https://doi.org/10.1016/j.jhazmat.2020.124504.

CC

Appendix

Specimen	Cc (%)	Cw (%)	Tc (day)	Sp (mm)														
				0.5	1	1.5	2	2.5	3	3.5	5	7	9	11	13	15	17	20
C06W50T07	6	50	7	46.24	53.50	51.08	48.12	45.17	42.48	38.71	28.50	18.28	11.02	11.83	11.56	9.68	8.60	6.18
C06W50T14	6	50	14	37.37	52.69	52.42	51.35	50.27	48.66	46.24	38.44	27.42	23.93	23.12	23.12	22.58	19.89	18.55
C06W50T28	6	50	28	68.95	70.31	67.59	65.68	62.95	59.96	56.14	38.43	23.16	14.72	10.63	11.45	9.81	7.36	5.72
C06W70T07	6	70	7	3.80	6.73	7.02	7.02	6.73	6.44	6.14	4.39	3.51	2.93	2.93	2.93	2.63	2.34	2.34
C06W70T14	6	70	14	7.21	9.70	9.95	9.70	8.95	8.46	7.71	4.23	2.49	3.73	2.98	3.23	2.74	1.99	2.49
C06W70T28	6	70	28	5.27	9.07	9.95	9.36	8.19	7.31	6.14	4.10	2.63	2.63	2.93	2.93	2.34	1.76	2.05
C06W90T07	6	90	7	2.59	3.17	3.46	3.17	2.88	2.59	2.31	1.73	1.44	1.15	0.86	0.58	0.29	0.29	0.29
C06W90T14	6	90	14	28.18	26.80	24.87	23.21	21.28	19.89	17.96	16.03	14.64	10.78	11.88	11.33	9.95	10.22	8.57
C06W90T28	6	90	28	15.58	27.52	24.20	22.22	20.56	19.23	17.57	13.93	10.28	8.29	6.96	5.64	5.64	4.64	4.97
C18W50T07	18	50	7	459.48	649.16	674.23	683.22	674.77	636.07	569.03	388.35	234.37	206.85	227.83	226.20	181.50	135.72	129.45
C18W50T14	18	50	14	817.58	1381.70	1482.54	1501.62	1482.54	1436.21	1359.90	1060.12	596.83	463.29	547.78	588.66	501.45	337.93	280.70
C18W50T28	18	50	28	610.09	1305.07	1803.76	1976.17	2015.96	2005.35	1912.51	1498.71	901.88	607.44	708.24	763.94	705.59	578.26	480.12
C18W70T07	18	70	7	184.23	277.16	293.51	285.33	276.61	267.62	255.63	201.12	120.18	55.87	53.96	76.03	79.03	62.95	26.16
C18W70T14	18	70	14	206.55	291.39	327.38	346.10	345.23	327.96	301.34	192.51	98.59	96.55	134.29	143.36	98.89	53.83	64.95
C18W70T28	18	70	28	217.11	360.12	393.56	395.29	374.24	345.99	312.26	207.88	106.39	103.80	131.19	127.73	89.67	59.68	83.61
C18W90T07	18	90	7	67.75	147.06	183.89	165.88	155.12	147.86	142.49	126.62	101.89	62.64	48.39	48.66	50.27	47.85	38.44
C18W90T14	18	90	14	231.53	192.77	180.42	171.50	167.73	160.18	152.29	127.94	101.53	80.26	78.89	82.66	83.01	81.64	67.23
C18W90T28	18	90	28	275.21	220.83	204.25	191.32	180.04	167.44	162.80	135.61	100.80	78.58	55.04	47.08	46.09	41.45	32.83
C30W50T07	30	50	7	673.27	1367.74	1634.74	1758.03	1803.06	1788.66	1739.45	1391.30	895.25	620.65	657.82	733.74	673.53	570.39	438.98
C30W50T14	30	50	14	863.02	1882.96	2591.87	2989.76	2967.34	2802.02	2247.22	585.62	439.92	297.01	353.05	437.12	448.32	316.63	271.80
C30W50T28	30	50	28	2035.14	3454.63	3879.40	3831.01	951.70	992.03	1008.16	849.54	290.35	220.45	371.00	551.13	424.77	190.88	204.32
C30W70T07	30	70	7	257.30	480.12	753.33	981.46	1010.63	1002.68	968.19	753.33	456.24	307.70	366.06	397.89	352.79	241.39	190.99
C30W70T14	30	70	14	557.04	1179.45	1349.97	1421.03	1429.55	1367.03	1267.56	971.98	548.52	457.57	557.04	562.73	500.20	375.15	397.89
C30W70T28	30	70	28	605.12	1392.61	1530.76	1588.79	1594.31	1544.58	1417.47	969.85	508.41	502.89	596.83	605.12	469.73	317.76	339.86
C30W90T07	30	90	7	291.13	418.34	474.66	490.07	489.23	479.71	463.73	397.89	291.41	185.21	192.50	224.72	227.52	203.99	153.83
C30W90T14	30	90	14	145.89	198.28	304.72	355.45	365.39	349.48	313.34	161.81	40.45	25.20	51.06	72.28	51.06	15.58	12.60
C30W90T28	30	90	28	454.30	745.30	742.33	712.63	700.76	691.85	677.00	579.02	418.67	273.18	166.28	151.43	163.31	157.37	133.62